ECOLE POLYTECHNIQUE FEDERALE DE LAUSANNE
SCHOOL OF LIFE SCIENCE

Master's project in Bioengineering and Biotechnology

A mechanical approach to study the bending of the primary cilium in response to fluid flow

Carried out in the Cell and Molecular Biomechanics Laboratory
Columbia University in the City of New York
Under the supervision of Prof. C.R. Jacobs

by
Florian Herzog

Under the direction of
Prof. Dominique Pioletti
In the Laboratory of Biomechanical Orthopedics

EPFL
Lausanne, 2010

Abstract

The primary cilium, a hair-like projection from the cellular membrane, is involved in fluid flow sensing. Bending the primary cilium is known to trigger several signaling pathways. In this study, the primary cilium is modeled as a thin beam undergoing large deflection due to fluid drag forces. For the first time, the bending response is analyzed with a model combining large angle rotations with the assumption of a linear drag force along the ciliary length. In addition, the initial curvature and the angle between the cell membrane and the cilium are integrated into the model. The model is applied on three dimensional confocal images of fluorescent cilia in living cells that are exposed to laminar shear flow. The coordinates of the cilia are computed by a simple and effective image processing algorithm. By fitting the equations of the model to the coordinates of the bent cilia, the flexural rigidity and the angle between the cilium and the cell membrane are estimated. The flexural rigidity of the primary cilium is approximately 10^{-23}Nm, but the values vary for different cilia, which suggests that the mechanical properties of the primary cilia are heterogeneous. Interestingly, the base of the cilium doesn't deflect under fluid flow which means that the primary cilium is firmly anchored. Using immunocytochemistry, the connections of the microtubule network to the base of the cilium could be resolved. The microtubules may provide the mechanical stability of the cilium. Incorporating a linear drag force and allowing a basal tilt is an important step towards a more realistic mechanical model of the primary cilium and towards more accurate values of its flexural rigidity. The model together with the imaging technique is a useful tool to study the mechanical behavior of the primary cilium and will eventually lead to new insight in the poorly understood mechanisms of mechanotransduction.

Keywords: Primary cilium, mechanotransduction, flexural rigidity, torsional stiffness, modeling

Contents

1 Introduction

Mechanical stresses modulate and orchestrate cellular responses from the very beginning throughout the entire lifespan of an organism. Evidence is growing that not only highly specialized cells, such as cells for hearing and touch, but virtually every cell is mechanoresponsive [14]. Cells have mechanical sensory capabilities and the ability to convert mechanical signals into a biochemical response. There are variety of different mechanical signals acting on cells, a multitude of proteins involved in signal transduction and the responses range from short term changes in the cytoskeletal arrangement to long term changes in gene expression. Often, multiple signaling pathways are activated by mechanical forces, and the orchestrated response enables the cell to adapt to changing mechanical conditions, which in turn modulates tissue morphology and remodeling.

The primary cilium is a specialized cellular organelle that has recently been implicated in mechanosensation. It is a hair-like projection from the apical cell membrane into the extracellular space present on the majority of mammalian cells. Its structure is based on nine doublet microtubules, which originate from the basal body and form a radially symmetric axoneme (see Fig.1). The primary cilium is connected to the cytoskeletal microtubules via the basal body and the basal feet. The basal body in turn is connected to the cell membrane by alar sheets and to striated rootlets, a filamentous, cytoskeletal structure.

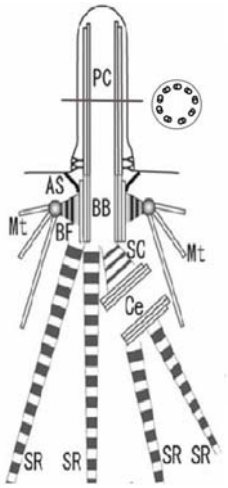

Figure 1: Structure of the primary cilium (PC). The primary cilium consists of 9 doublet microtubules, which originate from the basal body (BB) and form a radially symmetric axoneme. The basal body is linked to the cell membrane by alar sheets (AS) and to the cytoskeletal microtubules (Mt) by basal feet (BF). Striated rootlets (SR), a cytoskeletal filament, is also associated with the basal body. Image adapted from [11].

Although primary cilia have received little attention during most of the time since their discovery, it is becoming clear that they are a center of chemical and mechanical signal transduction during vertebrate development [8], in bone [33, 1], kidney and liver [9]. Dysfunction is associated with many diseases [18] such as cancer [21], polycystic kidney and liver disease [9], adiposity [10] and retinal degeneration [27]. A specialized protein transport system called intraflagellar transport mediates the assembly and dissociation of the primary cilium and the trafficking of ciliary proteins [31]. Among the variety of proteins present on the primary cilium, many signaling molecules localize to the ciliary membrane, including receptors for Sonic hedgehog, Wnt, platelet-derived growth factor, serotonin and somatostatin [1].

The mechanosensory role of the primary cilium was first demonstrated in renal epithelial cells. Fluid shear or micropipette induced bending of the primary cilium in MDCK cells leads to an increase of intracellular calcium [26]. This mechanosensory response is mediated by polycystins 1 and 2 in kidney cells. Both transmembrane proteins localize to the base of the cilium, and functionality of both proteins is required for the flow induced increase in intracellular calcium [23]. In bone, primary cilia are required for the dynamic fluid flow induced osteogenic and bone resorptive responses which is independent of Ca^{2+} flux and stretch-activated ion channels [20]. Further investigations showed that fluid flow leads to a decrease in intracellular cAMP which depends on the primary cilium, and on a molecular level on adenylyl cyclase isoform 6 and Gd^{3+}-sensitive channels and that this response mediates flow-induced COX-2 gene expression [16]. This suggests that the primary cilium mediates mechanosensitve signaling responses that are tissue specific.

Given the important role of the primary cilium in mechanosensation, it is surprising that only little is known about the mechanical properties of this structure. In contrast to the motile cilium, there are only few models of the primary cilium found in the literature. Schwartz *et al.* modeled the primary cilium as a thin elastic beam that deflects in response to fluid drag [30]. They used the Euler-Bernoulli beam theory and solved the differential equation with Maclaurin series. The major limitation of this model is the assumption of constant fluid velocity and drag, which doesn't agree with their experimental measurements of the fluid velocity in the vicinity of the cells. Liu *et al.* proposed a similar model, which considered more realistic fluid assumptions, but which was limited to small deflections [19]. A finite element model of the primary cilium was developed recently by Rydholm *et al.* [29]. In addition to an elastic axoneme, the ciliary and apical cell membrane was modeled as well. But there is only little known about the mechanical properties of the ciliary membrane, and the parameters of their model were obtained from whole cell experiments of red blood cells. Therefore, the model has to be refined and validated before accurate results can be obtained. Another general problem is that a finite element model is not able to determine the stress at a sharp edge, for instance between the ciliary and the cellular membrane.

Here, a novel mechanical model is proposed which simulates the bending of the primary cilium in response to fluid flow. It combines a realistic linear fluid velocity profile

with large deflections of a thin beam. In addition, the model includes new features such as allowing for a tilt at the base of the cilium and the initial curvature of the cilium without flow. Attempts were made to improve the estimation of the drag forces experienced by a deflected beam in three dimensions by computational fluid dynamics. Confocal microscopy is used to image fluorescently labeled cilia in living cells that are exposed to laminar shear flow in a parallel plate flow chamber. The images of the cilia under flow are then automatically processed and the three dimensional coordinates of the cilia are extracted. The goal of this study is to analyze the profiles of the primary cilia with the mechanical model. By comparing the actual bending profiles of the cilia with the simulations, the flexural rigidity of the primary cilium will be determined. With the powerful imaging technique and the image processing tools, the bending of the primary cilium in response to fluid flow is characterized in three dimensions. In addition, the structure of the base of the cilium is analyzed by immunocytochemistry.

2 Materials and Methods

2.1 Cell culture

Kidney epithelial cells from the inner medullary collecting duct (IMCD), which were previously transfected with a GFP somatostatin type 3 receptor fusion protein (eGFP-SSTR3) were cultured in tissue culture treated petri dishes with F12/DMEM 1:1 (Invitrogen, 11330), supplemented with 10% fetal bovine serum (FBS) (ATCC 30-2020)), 1% penicilin / streptomyocin (Invitrogen, 15140) and 200 μg/mL geneticin (Invitrogen, 11811) in a humified incubator with 5% CO_2 at 37°C. Geneticin was added to maintain selective pressure on the transfected cells. The fluorescent fusion protein localizes to the primary cilium and enables fluorescent imaging in living cells. For life-cell imaging, the IMCD cells were grown on 22x40 mm coverglasses to 60-80% of confluency and were then growth arrested by lowering the concentration of FBS to 0.5% for maximally two days.

2.2 Visualization of the plasma membrane

Wheat germ agglutinin (WGA) fluorescently labeled with Alexa 594 (Invitrogen W11262) was used to stain the cell membrane in living cells. Cells were washed with PBS and then incubated with 5 μg/mL WGA dissolved in Hank's buffered salt solution (HBSS) for 10 minutes at 37°C. After two quick washes with HBSS, cells were imaged immediately, because the fluorescently labeled lectin becomes endocytosed within 10-20 minutes.

2.3 Immunocytochemistry

Cells were seeded on 12mm 1.5 thick circular cover glasses in a 24 well plate at a concentration of 50'000 cells per well the day before staining. Cells were washed twice with prewarmed PBS, fixed with 4% paraformaldehyde for 15 minutes at room temperature (RT), and washed again three times with PBS. Next, cell membranes were permeabilized with 0.5% Triton X-100 for 5 minutes, followed by 3 washes with PBS. To prevent unspecific binding, the cells were blocked with 3% bovine serum albumine (BSA) dissolved in PBS fro 20 minutes. Primary antibodies were then incubated overnight at 4 °C. Optimal dilutions were determined by titration: monoclonal rabbit anti alpha tubulin 1:1000 (Abcam, ab52866), monoclonal mouse anti gamma tubulin 1:1000 (Invitrogen, T6557), monoclonal human anti rootletin 1:1000 (Acris, AM00479PU-N). Excessive antibodies were removed by 3 washes with PBS lasting 20 minutes each. Next, secondary antibodies, donkey anti rabbit IgG Alexa 555 (Invitrogen A31572), donkey anti mouse IgG NL 637 (R&D Systems, NL008) and goat anti human IgG Alexa 633 (Invitrogen A-21091) were added at a dilution of 1:200 and incubated for 1 hour at RT, followed by 3 washes with PBS for 20 minutes each. Both primary and secondary antibodies were dissolved in PBS with 0.5% BSA.

Cover slides were mounted on precleaned glass slides with Prolong AntiFade Gold (Invitrogen, P36930) mounting medium, that was cured at RT, protected from light,

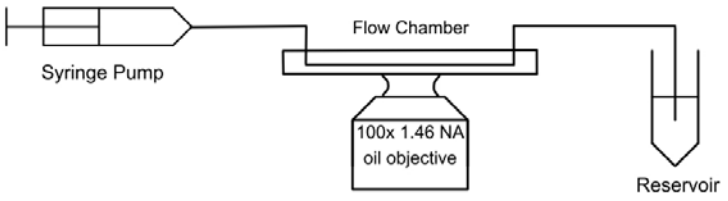

Figure 2: The flow set up. The laminar flow chamber is connected to a syringe pump, which administers a well controlled flow rate. A reservoir is connected to the outlet of the chamber, such that positive and negative flow rates can be applied on cells.

for 24 hours before sealing the coverglass with nailpolish. For immunocytochemistry with the rootletin antibody, ice-cold methanol fixation for 10 minutes was used instead of paraformaldehyde fixation and permeabilization with Triton X-100.

2.4 Applying shear stress on cultured cells

Well controlled fluid shear stress was applied on cultured IMCD cells with the laminar flow chamber RC-30 (Warner Instruments) connected on one side to a syringe pump (Genie Plus, Kent Scientific) with a 1 mL Hamilton gas tight syringe and a reservoir at the other (see Fig. 2). The RC-30 flow chamber is designed for confocal imaging systems. It consists of a circular mount, in which a gasket can be placed between a top and a bottom coverslip, with the dimension 30x24 mm^2 and 40x24 mm^2 respectively. The gasket has a thickness of 250 μm and a narrow channel with a width of 3.2 mm. The flow in the chamber is steady and the liquid is assumed to be Newtonian. The wall shear stress for the flow between infinitely wide parallel plates depends linearly on the flow rate:

$$\tau_{wall} = \frac{6\eta Q}{bh^2} \tag{1}$$

where τ_{wall} is the shear stress in [Pa], Q the flow rate in [mm^3/s], η the dynamic viscosity [Pa s], b the width [mm] and h the height of the channel in [mm]. The viscosity of the medium was assumed to be 10^{-3} Pa s, which is the viscosity of water at 20°C. In a finite flow chamber, the shear stress is not uniform along its width, but decreases in the vicinity of the edge [2]. Therefore, cells were imaged only in the center of the channel. The flow rate Q was set between 150-500 μL/min, corresponding to shear stresses of 75-250 mPa. In order to avoid thermal gradients which lead to a focal drift during imaging, the flow chamber was assembled and put into the microscope room 1 hour before imaging.

2.5 Confocal laser scanning microscopy

High resolution images of the primary cilium in living cells, and other subcellular structures on fixed cells were taken with the Leica SP5 confocal laser scanning mi-

Table 1: Parameter Values

Parameter	Symbol	Value	Unit
Flow rate	Q	150-500	μL/min
Fluid viscosity	η	0.001	Pa s
Fluid density	ρ	1000	kg/m^3
Channel width	b	3.2	mm
Channel height	h	0.25	mm

croscope, equipped with a 100x, 1.46 NA oil immersion objective and a motorized Super Z Galvo stage. For live cell imaging of fluorescent cilia, the resonant scanner was used with bidirectional scanning, which allows high speed imaging in three dimensions with a voxel scanning rate of 8000Hz. The resolution of a confocal microscope is approximately $Res_{xy} = \frac{0.44\lambda}{NA}$ and $Res_z = \frac{1.5n\lambda}{NA^2}$ in the lateral and axial direction respectively [37]. The resolution with the given microscope and GFP are $Res_{xy} = 151nm$ and $Res_z = 534nm$, as $\lambda = 500$nm and the refractive index of the immersion oil is n=1.518. An Argon laser, with wavelength $\lambda = 488$nm was used to excite the GFP fusion protein, and the cilia were scanned with a lateral voxel dimensions of about 50nm and a voxel height of 100nm. The scan of a single cilium takes about 1-2s. To decrease fluctuations, the cilia were scanned 20 times consecutively. For immunocytochemistry, the images were taken without the resonant scanner, and the HeNe 543 and 633 lasers were used to excite the Alexa 555, Alexa 633 and NL637 labeled secondary antibodies.

2.6 Image Processing

Deconvolution and 3d reconstruction. Confocal images of the tubulin network and the membrane stain together with the fluorescent cilia were deconvoluted with Huygens Deconvolution Software (Scientific Volume Imaging, SVI) using the classic maximum likelihood estimation algorithm. The fluorescent cilia with the membrane stain were reconstructed in three dimensions with freeSFP (SVI) which implements the simulated fluorescence process algorithm.

Detect and extract ciliary profiles. An image processing script was developed with the Matlab image processing toolbox to extract the three dimensional coordinates of the cilium from the confocal images. As the cilium is almost parallel to the optical axis, it appears as a dot in the xy plane (see Fig. 3). The eGFP-SSTR3 fusion protein localizes to the ciliary membrane. The ciliary membrane as such can't be resolved with the given imaging system, as the diameter of the cilium (about 200nm) is too close to the resolution limit of the laser scanning confocal microscope, even with the 100x 1.46 oil immersion objective. The signal recorded by the detector is a convolution of the different fluorescent signals of the eGFP-SSTR3 molecules with the point spread function of the imaging system. The resulting image is similar to a Gaussian distribution, which will be used for the further image processing.

The confocal images of the cilia in 4d (xyzt) are saved as TIFF files together with

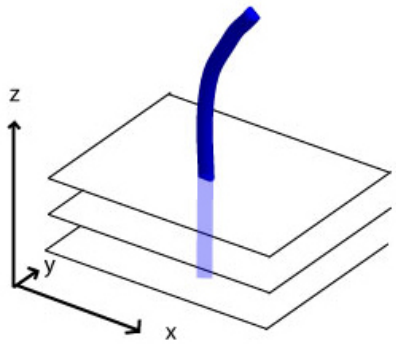

Figure 3: Imaging of the primary cilium. The primary cilium appears dot-like in the xy-plane of a confocal image.

the metadata in a XML file by the Leica LAS AF software. A Matlab code reads the metadata and acquires the dimensions and the pixel size of the images. Then, each individual image is read and converted into a 8bit greyscale image and a Gaussian filter, with parameter $\sigma = 200$ nm and dimensions of 4σ x 4σ is used to decrease noise (a typical mask is shown in Fig. 4 D). Mathematically, the convolution of the image with the Gaussian filter mask is equivalent to a correlation with the Gaussian, because of the symmetry of the mask. Next, pixels exceeding a manually chosen threshold are sampled, and if more than 10 pixels were sampled at a given height z, the x and y components of the sampled pixels were averaged and taken as the center of the primary cilium. The result of the filter and the threshold are shown for a typical cross section of a cilium in Fig. 4 A-C.

To filter the fluctuations of the primary cilium, an average coordinate of the cilium was obtained by averaging the xy coordinates through time (usually 20 z-stacks imaged during 30s), if more than half of the scans satisfied the criterium of being a ciliary cross-section. The three-dimensional coordinates of the cilium are then projected into the xz plane, with x being the direction of flow and z the axis perpendicular to the cell membrane, which serves as an input for the mechanical model.

2.7 Computational fluid dynamics

For the three dimensional simulation of the fluid flow around a cylinder, the computational fluid dynamics program of the finite element software ADINA, version 6.6.2 was used. The computer used for simulation was equipped with four 2.8 GHz processors and 7 GB RAM.

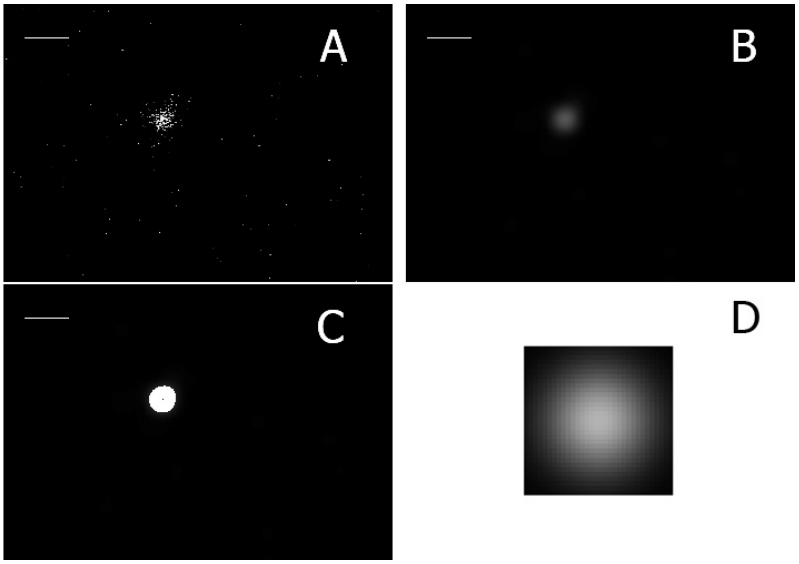

Figure 4: Image Processing. (A) Original noisy image of a cross section of a primary cilium imaged with the resonant scanner. (B) Image filtered with Gaussian low pass filter. (C) Pixels exceeding the threshold are shown in white, and their mean position is indicated with a black point, which is used as the coordinate of the cilium. (D) shows a typical enlarged Gaussian filter mask. Scale bar 1 μm.

3 Model development

A part of the following theoretical considerations and the numerical implementation was previously developed in the Cell and Molecular Biomechanics Laboratory by Jaj Geraedts. The theory and implementation of the initially curved cilia, the elliptical cylinder approximation, the three dimensional fluid simulations and the whole image processing part are my major contributions to this model. In addition, the fitting algorithm was changed together with some other corrections and changes in the script of J. Geraedts.

3.1 Thin elastic beam

The primary cilium is modeled as a thin, elastic, homogeneous beam with uniform cross-section along its length. From the Euler-Bernoulli beam theory we know that

$$\frac{d\theta}{ds} = -\frac{M(s)}{EI} \tag{2}$$

where s is the position along the beam starting at the free end, θ the angle between tangent and vertical as shown on Fig. 5A, M the bending moment, E the Young's modulus of elasticity and I the second moment of inertia. The product EI is called flexural rigidity, which describes the effective stiffness of the beam, considering both material and geometrical factors.

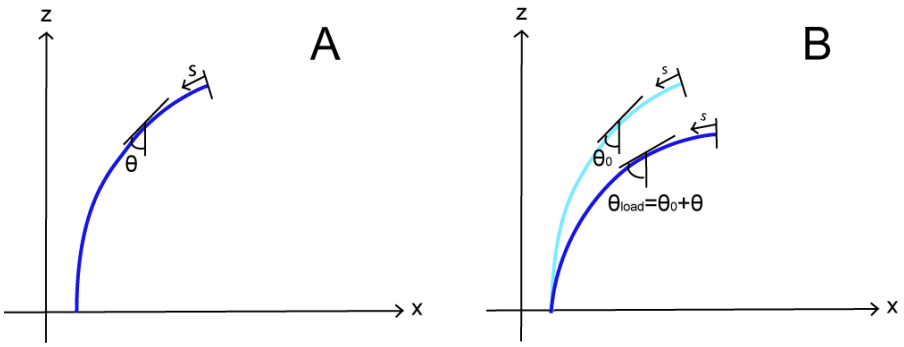

Figure 5: Illustration of the coordinate systems used.

If the beam is subject to a continuous load perpendicular to its long axis, it follows that the derivative of equation (2) with respect to s yields

$$\frac{d^2\theta}{ds^2} = -\frac{w(s,\theta)}{EI} s\cos(\theta) \tag{3}$$

where w is the load per unit length [12].

The bending moment M must therefore be:

$$M(s) = \int_0^s w(\bar{s},\theta)\bar{s}\cos(\theta)d\bar{s} + \mathrm{fct}(\theta) \tag{4}$$

Note that the bending moment at a given point s is equal to the integral of the moments from 0 to s. Here, the moment at a given element s with length ds is $m(s) = swcos(\theta)ds$. This is only an approximation, because the effective lever arm is the linear distance l and not the distance s along the beam (see Fig.6). This approximation will lead to errors which increase with increasing deflection. This error was only discovered by the end of the project and wasn't corrected for the simulations. Nevertheless, the problem can be solved by starting with $l = s$, and then update the value of l according to the previous beam profile in the Cartesian coordinate system, much like the drag on a given element is updated during the fitting process.

Equation (3) can be rewritten in a non dimensional form by introducing $\kappa = wL^3/EI$ and $\bar{s} = s/L$ with L being the length of the beam [12].

$$\frac{d^2\theta}{d\bar{s}^2} = -\kappa(\bar{s},\theta)\bar{s}\cos(\theta) \tag{5}$$

The boundary conditions are such that the angle between vertical and the tangent of the beam is a given angle θ_{base} at the fixed end and the bending moment at the free end is zero:

$$\theta = \theta_{base} \quad \text{at} \quad \bar{s} = 1 \tag{6}$$

$$\frac{d\theta}{d\bar{s}} = 0 \quad \text{at} \quad \bar{s} = 0 \tag{7}$$

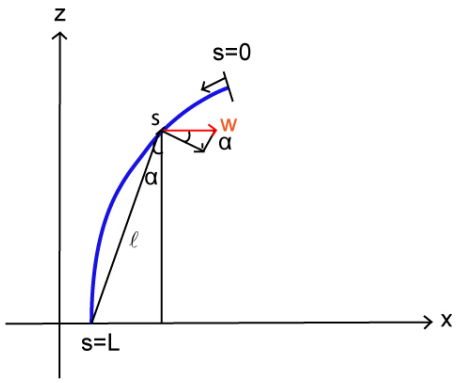

Figure 6: Bending moment

So far, the beam is considered straight if no load is applied. It was observed that the the primary cilium may have an initial curvature. For this case, the equation (4) can be adapted as follows (see Figure 5):

$$M(s) = \int_0^s \bar{s} w cos(\theta + \theta_0) d\bar{s} \tag{8}$$

The bending moment depends on the angle between the direction of the load (the horizontal) and the tangent of the beam $(\theta_0 + \theta)$, whereas the angle in equation (2) refers to the change in angle due to the load, θ. It follows that

$$\frac{d^2\theta}{d\bar{s}^2} = -\kappa \bar{s} cos(\theta + \theta_0) \tag{9}$$

As equation (5) has never yielded an analytical solution, a numerical approach is used to solve the differential equations. The second order differential equation can be decomposed into a system of two first order equations.

$$\frac{d\theta_1}{d\bar{s}} = \theta_2 \tag{10}$$

$$\frac{d\theta_2}{d\bar{s}} = -\kappa \bar{s} cos(\theta_1 + \theta_0) \tag{11}$$

This system of differential equations can be numerically integrated to find $\theta(\bar{s})$. The xy coordinates can then be obtained:

$$x(s) = L \int_0^s cos(\theta + \theta_0) d\bar{s} \tag{12}$$

$$y(s) = L \int_0^s sin(\theta + \theta_0) d\bar{s} \tag{13}$$

3.2 Fluid flow

Hydrodynamic drag is the force leading to the bending of the primary cilium. It was experimentally observed and theoretically predicted that the flow in the vicinity of cells in a laminar flow chamber is almost linear, with zero velocity at the fluid-cell interface [30]. Previous studies have shown that the cilium deflect at tip velocities in the order of 50 μm/s [30]. The flow around a thin cylinder, whose diameter $d = 0.2$ μm, at a fluid velocity of about $v = 50$ μm/s is called creeping flow, as the Reynolds number, defined as $Re = \rho v d/\eta = 10^{-4}$ is much smaller than one. This means, that viscous forces dominate largely over inertial forces. To determine the drag acting on the cylinder at a given height z, a 2d approximation based on the circular cross-section of the cylinder and the local fluid velocity $v(z)$ can be used. When the beam bends or rotates, the cross section of a cylinder in the plane of uniform velocity changes from circular to elliptical. Drag on elliptical cylinder was therefore estimated and to analyze the three dimensionality of the flow, an attempt to simulate a tilted cylinder was done by computational fluid dynamics.

3.2.1 Drag on a circular cylinder

The motion of a fluid can be described by the Navier-Stokes equation. As the Reynolds number for the given problem is very small, one could neglect the inertial terms of the Navier-Stokes equation which leads to the Stokes equation. Unfortunately, there is no analytical solution of a body immersed in a unlimited viscous incompressible fluid, which motion is described by the Stokes equation. This problem is known as the Stokes-paradox [32], which resulted from the neglect of inertia terms, according to Oseen [4]. Oseen added a linear inertial term to the Stokes equation in order to overcome the Stokes-paradox. The linear inertial term is small close to the cylinder, but becomes important in the far field. Lamb found an analytical first order approximation of flow around an infinite, circular cylinder and an expression for the drag forces using Oseen's equation [17]:

$$w = \frac{4\pi\rho v^2 d}{Re(2.002 - ln(Re))} \tag{14}$$

This equation is valid at low Reynolds number, and was experimentally validated [5, 34]. We assume that the fluid velocity is zero at $z = 0$ and increases linearly with z. Actually, the flow profile is parabolic and homogeneous in the center of the parallel plate flow chamber [2], but as the height h of the flow chamber is much larger than the length of the cilium, the linear approximation is reasonable. For the given dimensions, the drag per unit length w is almost linearly dependent on the height z (see Fig. 7). Therefore, the drag per unit length is approximated as a linear function $w(z)$.

3.2.2 Elliptical cylinder approach

When the cilium bends, the initially circular cross section becomes elliptical in the plane of uniform flow (xy-plane). To study if this change in cross section has an effect

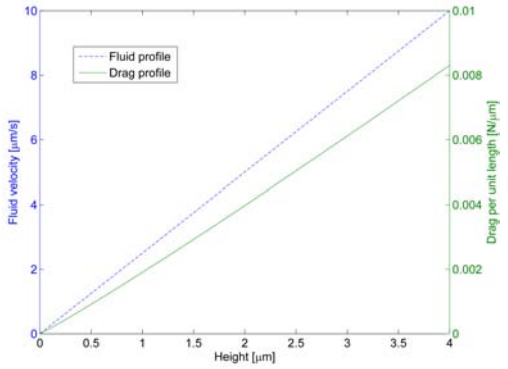

Figure 7: The drag per unit length depends almost linearly on the height z from the no-slip boundary.

on the drag, the solution of Oseen's equation for elliptical cylinders was used [13]. The drag coefficient C_D is

$$C_D = \frac{16\pi}{Re}\frac{1}{2S+1-\sigma^2}[1-\frac{Re^2}{32(1+\sigma^2)^2}\{S+\frac{1}{2}(\sigma^2+\sigma^4) + \frac{1}{24}\frac{1}{2S+1-\sigma^2}(15+4\sigma^2-18\sigma^4+12\sigma^6-\sigma^8)\}] \tag{15}$$

with Re the Reynolds number, $\sigma = \sqrt{(a-b)/(a+b)}$, a the major and b the minor axis, $S = log(8(1+\sigma^2)/Re) - y$ and y the Euler constant. The ratio σ can easily be calculated for a tilted cylinder, and the drag per unit length D is in the case of a cylinder

$$D = C_D\frac{v^2\rho d}{2} \tag{16}$$

The results for the geometry of the cilium at a $Re = 10^{-2}$ are shown and compared to the solution for a circular cylinder by Lamb in Fig. 8. The drag decreases only about 2% when the cylinder is tilted from 0 to 45°. This effect was considered negligable and the circular cylinder approach is sufficient to describe the drag on a bent cilium in 2d.

3.2.3 3d Computational Fluid Dynamics Simulation

The fluid flow around a bent beam is a three-dimensional problem. The local velocities around the beam will not only have x and y components, but also a z-component due to the inclined boundary. Computational fluid dynamics were used to determine if this z-component of the velocity introduces changes in drag compared to the 2d approximation. The goal was to establish a relationship between the drag and the angle of incidence of the flow with respect to the cylinder. The finite element software ADINA, version 8.6.2 was used to simulate the fluid flow around a circular cylinder.

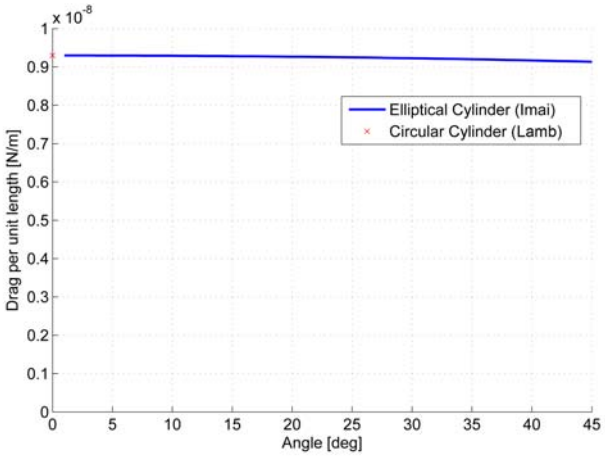

Figure 8: The drag on a circular cylinder compared to a cylinder tilted form 0-45° at low Reynolds number. Tilting the cylinder in direction of flow has only little effect on the drag in 2d.

The fluid flow was simulated within a box filled with tetrahedral fluid elements, with a defined inlet velocity v=10^{-5} m/s at one face, and slip boundary conditions at the bottom, the top and the lateral boundaries. The cylinder, with diameter $d = 10^{-3}$m and a no-slip condition at its boundary, was placed in the center of the computational box with a height equal to the height of the computational domain. The fluid density was assumed to be 1000 kg/m^3 and the viscosity 10^{-3} Pa s, such that the Reynolds number becomes 10^{-2}. This value was chosen because it is much smaller than one and a smaller value was avoided, because the simulations may converge slowly at low Reynold's numbers. The results can be extrapolated to lower Reynolds numbers, because the physical laws won't change and the ratio between the drag coefficient at 0° over the drag coefficient at a given angle should remain constant at different, but small Reynold's numbers.

The simulation has to be mesh and domain independent and should be consistent with the analytical solution of a circular cylinder (Equation (14)) when the cylinder is not inclined. It was observed that the drag depends highly on the width of the computational domain, but only little on the number of fluid elements. The dependence of the drag on the ratio width over diameter is shown in Fig. 9. The width of the computational domain has to be 1000 times larger than the diameter. Only at this ratio, the drag becomes close enough (10%) to the solution of equation (14). The model is validated, but the high ratio made it difficult or even impossible to run simulations for an inclined cylinder. The computational power available was not sufficient to simulate the drag for cylinders tilted at different angles, because the height of the domain had to be incrased to avoid boundary effects from the top and the bottom face and the number of fluid elements necessary to form a good mesh exceeded 5 x 10^6 elements. Unfortunately, the three-dimensionality of the flow could not be resolved and included into the model.

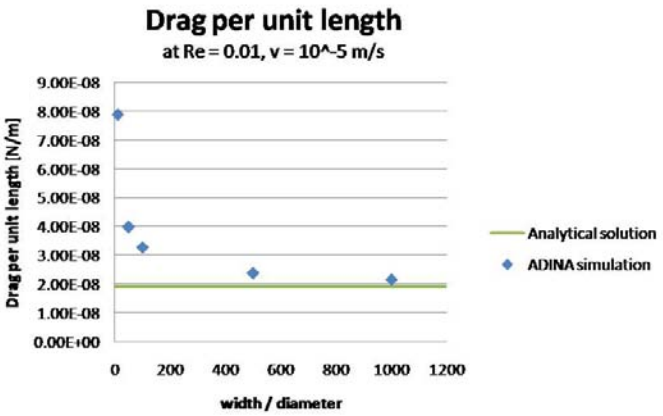

Figure 9: The ADINA simulation of the drag on a circular cylinder compared to the analytical solution

3.3 Numerical implementation, fitting algorithm

The differential equation of the beam, together with the linear drag forces $w(z)$ are fitted on the reference points of the cilium by adjusting EI and θ_{base} such that the error between the solution and the reference points becomes minimal. First, the reference points of the cilium under static condition are computed from the confocal images, as well as the reference points of the cilium under fluid flow (see Materials and Methods section). The coordinates of the cilium are rendered non-dimensional by a division by the length of the cilium. To determine the length, a 4th order polynomial was fitted on the reference points and the distance was estimate according to this fit. The profile of the cilium with no load, $s_0(\theta_0)$, is needed for the estimation of θ_0. It is obtained by the same fitting process described below, but with arbitrary values. This has no physical meaning, but allows to accurately estimate $s_0(\theta_0)$.

The fitting process starts with an initial guess for θ_{base} and κ_{tip}, which is the value of the non-dimensional parameter $\kappa = wL^3/EI$ in equation (5) at the height L. Changing κ_{tip} is equivalent to change EI, as L and w_{tip} are known and constant. With this initial guess, and with a linear load profile that is zero at $z = 0$ and κ_{tip} at $z = L$, the differential equations are solved with the standard boundary value problem solver bvp4c in Matlab, which implements a three stage Lobatto approach with automatic adaptive meshing and error control. The resulting profile $s(\theta)$ can be transformed into the xy plane by numerical integration of equation (12) and (13). The load at a given point s of the beam depends on the height z in the xz-plane, and this height z is different from the initial configuration. Therefore, the load $w(s)$ has to be updated according to the profile $s(\theta)$ in the Cartesian coordinate system and the differential equations are solved again, until the mean distance between two consecutive solutions becomes less than given tolerance. Next, the value for κ_{tip} is changed according to

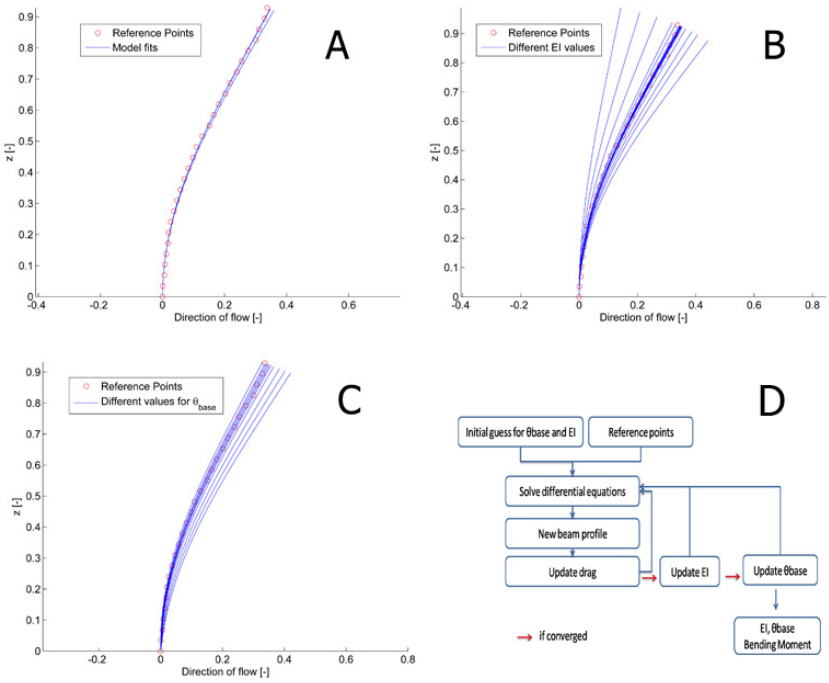

Figure 10: The numerical implementation and the fitting Process. (A) The drag is updated at each iteration according to the new beam profile. (B and C) The values of EI and θ_{base} are varied until the average distance between the reference points and the solution falls below a certain tolerance. (D) The flow chart of the fitting algorithm.

$$\kappa_{tip}^{n} = \kappa_{tip}^{n-1} + (d)stepsize^{n} \tag{17}$$

If the error between the reference points and the solution increases, the direction d changes and the step size is divided by two. The iteration is stopped when the step size becomes smaller than an accepted tolerance. Then, θ_{base} is fitted by the same optimization process. The process of the fitting algorithm is depicted in Fig. 10 D and the solutions for different updates of the load, different values for κ_{tip} and θ_{base} are shown in Fig. 10 A, B and C respectively.

In the end, the EI value can be computed by $EI = w_{tip}L^3/\kappa_{tip}$ and the bending moment at the base is obtained by the following discrete sum

$$\sum_{s=0}^{L} lwcos(\alpha)ds \tag{18}$$

where l is the linear distance between $s = L$ and s, w the force per unit length acting on an element s of length ds and α is the angle between l and the vertical (see Fig. 6).

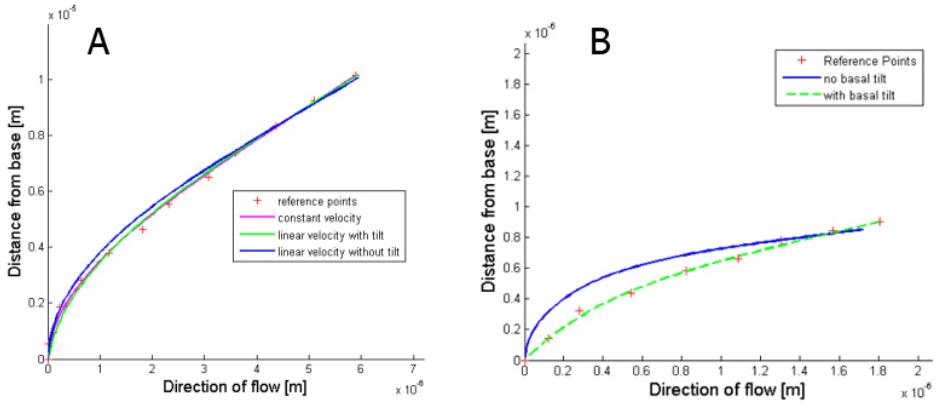

Figure 11: The effect of different model assumptions. (A) The fits obtained with a constant velocity, linear velocity and the linear velocity with tilt are shown. The fitted profiles are very similar, but allowing for a basal tilt leads to a slightly better fit (profile of the cilium from [30]). (B) Shows the profile of a highly bent cilium (from [20]), where the effect of the fitted angle at the base is more drastic. Allowing the base to tilt increases the accuracy of the fit.

4 Results

4.1 Validation and effect of model assumptions

The model was validated by using published data of a bent primary cilium from Schwartz *et al.* [30] and by comparing the resulting EI values. Schwartz *et al.* used Maclaurin series to solve equation (3) and assumed constant drag forces along the cilium. They reported EI values of 1.4-1.6x10^{-23}Nm^2. After modification of our model, where an initially straight cilium was considered and the drag forces were kept constant in order to meet their assumptions, an EI value of 1.24x10^{-23} Nm^2 was obtained. Assuming a linear drag profile, the EI value decreases to 0.50x10^{-23}Nm^2, and by fitting the angle at the base θ_{base} in addition to the linear velocity profile, the EI increases slightly to 0.60x10^{-23}Nm^2. The fitted beam profiles are shown in Fig. 11A. All models with the different assumptions are able to fit the reference points of the bent cilium and the difference between different fits is small. Allowing the base to rotate improves the fit slightly in Fig. 11A, but the effect is more important for a highly bent cilium, as shown in Fig. 11B.

4.2 Ciliary embedding

The relative position of the cilium with respect to the cell membrane was assessed by confocal imaging of living cells, which express eGFP-SSTR3 and which are stained with a common fluorescent cell membrane dye. Usually, the cilium is located at the top of the cell, projecting into the extracellular space (Fig. 12 A). The length of the cilia of IMCD cells is around 2-4 μm and the cilium can be tilted or curved, even if no load

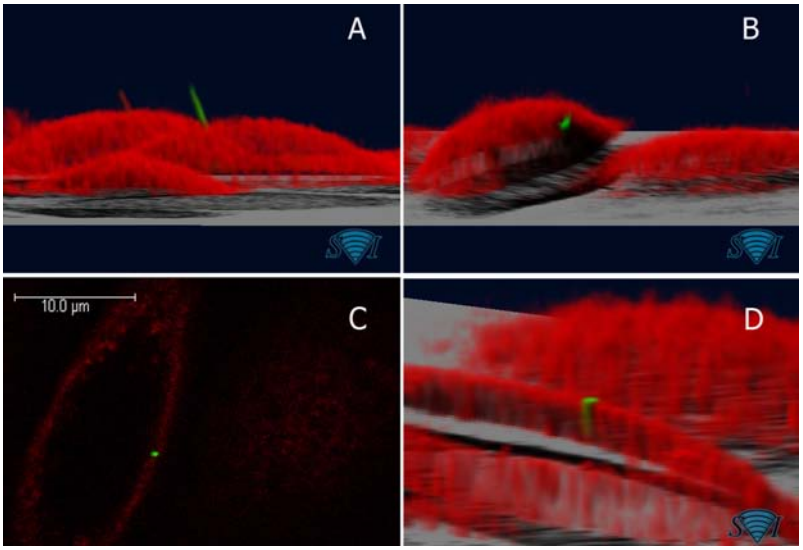

Figure 12: The position of the primary cilium on a cell. The cilium is seen in green (GFP-SSTR3) and the cell membrane in red (WGA-Alexa594). Images A, B and D are 3d reconstructions of deconvoluted images. (A) The primary cilium is usually at the top of the cell, projecting into the extracellular space. (B) In some cases, the primary cilium is small and embedded in the cell membrane. (C) is an original confocal image of cilium B which shows that the cilium is embedded in the cell membrane, and (D) is a 3d reconstruction with the data from (B), where the cell was cut at a certain height in order to visualize the embedded cilium.

is applied (Fig. 12 A). Interestingly, a very different position was observed for a small cilium (Fig. 12 B-D). This cilium is located at the side of the cell partially embedded in the cell membrane. The fluorescent signal of the transmembrane fusion protein is seen within the cellular membrane, which suggests that the membrane at the ciliary base forms an invagination (Fig. 12C and D). The fluid flow and the drag forces acting on the small, embedded cilium must be very different compared to the long cilium at the top of the cell, because of the steep cell membrane and the partial embedding. The longer cilia is not embedded and emerges directly form the cell membrane. To avoid misleading interpretations of the bending of the primary cilium, only long cilia at the top of the cell were considered for the comparison with the model.

4.3 Primary cilia length in growth-arrested IMCD cells

To study the effect of inhibiting cell proliferation on cilia length, IMCD cells were growth arrested by serum starvation, i.e. by culturing the cells with serum-free media. The length was assessed before serum starvation, at 1 and at 2 days of serum starvation. The results are shown in Fig. 13. The average length of the cilium slightly increases during serum starvation. After two days of serum starvation, no cilium was found with a length smaller than 2 μm, and the longest cilium was also found in this group, which was 4.5 μm long. However, no statistical significance between the means of each

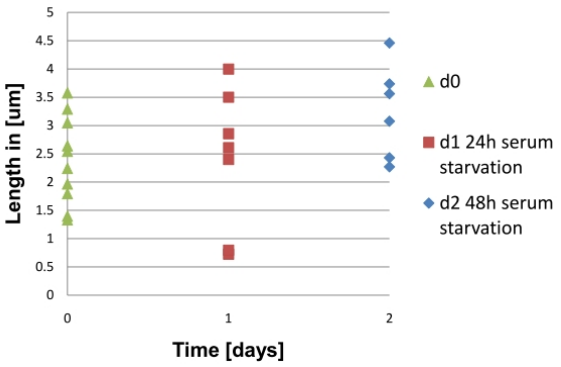

Figure 13: Cilia length seems to increase in growth arrested IMCD cells. The length of the cilia was measured on day 0, day 1 and day 2 after serum starvation (0% FBS).

group was found with a one-way ANOVA (P-value = 0.19). By increasing the number of data points, the increase might become statistically significant. Nonetheless, cells were growth arrested for two days for the bending analysis, because not only the cilia seem to be longer, but they are also likely to be more mature.

4.4 Fluctuations

Imaging with the high-speed resonant z-scanner revealed fluctuations of the primary cilium. The side-view of a cilium imaged 12 times within 25 seconds under static conditions is shown in Fig. 14. External vibrations were minimized and the cells were put into the microscope room one hour prior to imaging to avoid thermal gradients. For visualization, noise was decreased by a Gaussian filter and the average y intensity was projected into the xz plane. The movement of the cilium is better seen if the images are animated. The three-dimensional coordinates of the same cilium were obtained by further image processing and plotted in Fig. 15. The base of the cilium moves more in the y than in the x direction. This lateral movement may correspond to a cellular movement or an imaging artifact. On top of this lateral movement, the fluctuations appear more pronounced at the tip of the cilium than at the base.

A candidate source of the observed fluctuations are thermal forces. To test this hypothesis, we assume that the primary cilium is a flexible polymer. We would expect that

$$< cos(\Delta\theta) >= e^{-\frac{s}{L_p}} \tag{19}$$

where the brackets indicate the expectation value,$\Delta\ \theta$ the angle between the tangent at a point s and the tangent at point $s = 0$, s the position along the polymer and L_p the persistence length. The persistence length is a measure quantifying the stiffness of a long polymer and corresponds to the length over which the correlation of the tangent is lost. The flexural rigidity is related to the persistence length by the following equation.

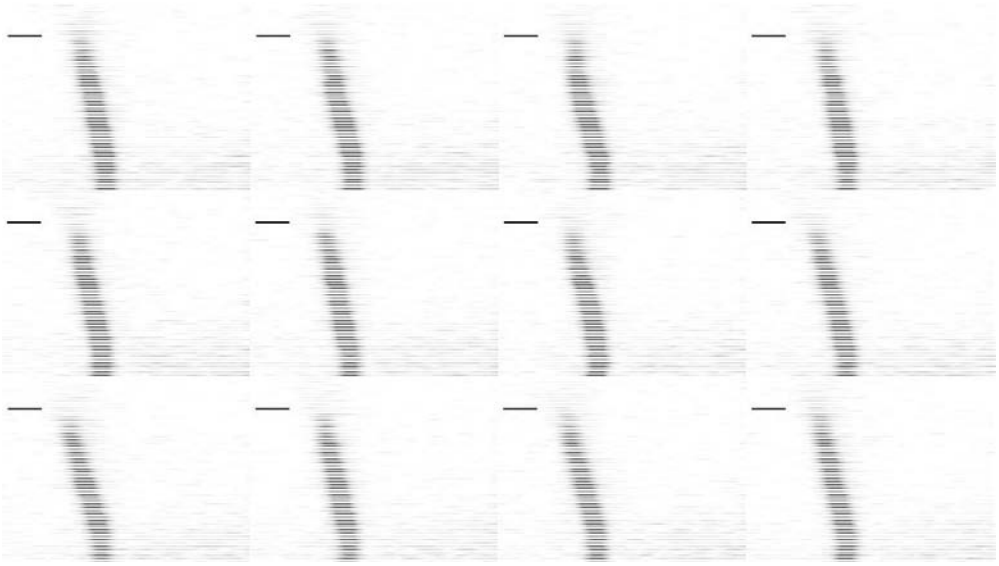

Figure 14: Time sequence of a cilium, side view. Average y intensities were projected into the xz plane after noise reduction with a Gaussian filter. The cilium fluctuates and seems to oscillate. Time step between consecutive images is 1.5s, scale bar 1 μm.

$$L_p = \frac{EI}{kT} \tag{20}$$

with k the Boltzmann constant and T the temperature. If the fluctuations are thermal, the measurements would provide a mean to estimate the flexural rigidity of the primary cilium. This method was indeed used by others to determine the flexural rigidity of microtubules or actin filaments [7]. If the persistence length is much longer than the length of the cilium, s/L_p becomes very small and we can approximate the exponential.

$$< cos(\Delta\theta) > \approx 1 - \frac{s}{L_p} \tag{21}$$

Using the data from 15, we can measure the tangent at the base which is approximately $\pi/2$ and at the tangent at the tip varies between $\pi - 0.1$ and $\pi - 0.3$ rad. The equation (21) yields

$$< cos(\Delta\theta) > \approx 1 - \frac{s}{L_p} \approx 0.97 \tag{22}$$

at $s = 4\mu m$. The persistence length is therefore 133 μm. The cilium consists of nine doublet microtubules, so we would expect a persistence length at least nine times longer than the one of a single microtubule. According to Pampaloni *et al.*, the persistence length of a microtubule with a physical length of 4 μm is $L_p^{Mt} = 200$ μm [25], which

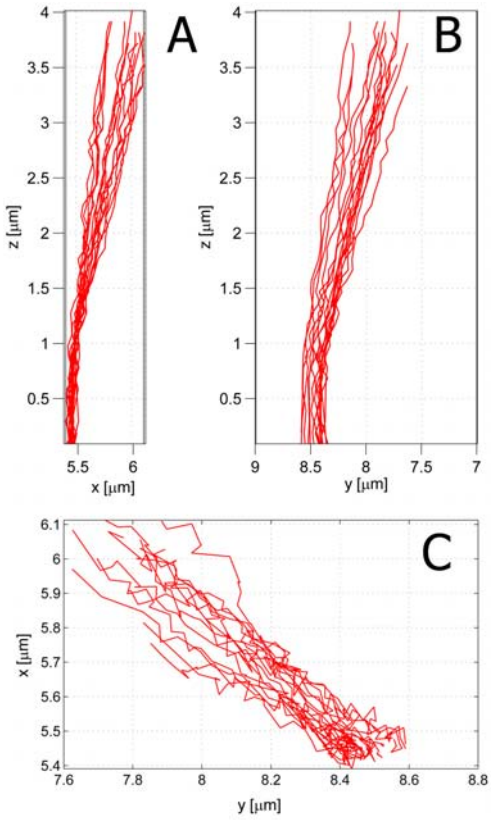

Figure 15: Three-dimensional coordinates of the cilium shown in Fig. 14 were obtained by image processing. The fluctuations are more pronounced in the y direction than in x, and apparently higher at the tip than at the base.

is larger than the estimated value obtained for the cilium. We can therefore exclude thermal fluctuations to be the reason of the fluctuations.

Another possible source of fluctuations are movements of the cell. In this case, we would expect to see a time dependence of the position, and the phase of the oscillations at the base should correlate with the oscillations at the tip. No clear time dependency was found, and no correlation between the phases. The sampling frequency might be too low for this analysis, so we can't exclude cellular movements from this data yet. Other possibilities are external vibrations that are transmitted to the sample or inaccuracy of the image processing. The external vibrations were minimized, but can't be completely avoided.

4.5 Flexural rigidity of the primary cilium

By fitting the model to the profiles of the cilia from the confocal imaging, the flexural rigidity and the angle at the base is be estimated. Unfortunately, only few data were obtained, and the results are variable. Figure 16 shows the profile of four different cilia without flow, with a flow rate $Q = 300$ μL/min and the fitted beam profile from the model. The given flow rate corresponds to a fluid shear stress of 150mPa. The cilia were imaged 20 times within 30 seconds in both conditions, and average coordinates were used for the analysis. The coordinates of the cilia form relatively smooth lines, and the model is able to simulate the bending profile very well.

The first important result is that the base of the cilium doesn't tilt. The tangent at the base of the cilium in the static condition is in all four cases almost identical to the tangent of the loaded cilia. The cilium forms an angle close to 90° with the cell membrane, which doesn't change when a load is applied (seeΔ θ in table 2). The bending moment at the base is not sufficient to induce a tilting.

The flexural rigidity of individual primary cilia vary largely. The values of the four cilia shown in Fig. 16 are listed in table 2, with values between $10^{-22} - 10^{-24}$ Nm^2. The average flexural rigidity is in the order of 10^{-23}Nm^2, which is the same as the one reported previously by Schwartz *et al.* [30]. Only small changes in deflection lead to a large change in the estimation of the flexural rigidity, which makes the measurements very sensitive. The observed deflections under flow were variable for different cilia, and no apparent correlation between length and flexural rigidity was found.

The length of the deflected cilia appear between 0.3-1.1 μm smaller than the unloaded cilia (ΔL in table 2). This change in apparent length was not considered in the simulation, as the non-dimensional coordinates were used. The change in apparent length is probably due to photobleaching. The fluorescent signal intensity decreases, and therefore, the signal to noise ratio becomes worse after a few scans of the same cilium. It becomes more difficult to estimate the coordinates of the cilium, and as the intensity decreases, the fewer slices are considered as part of the cilium. One could improve the image processing by lowering the threshold for later scans, which is difficult as the noise is relatively high even at the first scans, or the exposure of the fluorophores to the laser could be lowered. This can be done by decreasing the number of scans per condition, by lowering the laser power or by increasing the sampling size. The first option will increase the sensitivity to fluctuations and the second was already considered and minimal laser power was used. By choosing ten scans per condition, and by increasing the sampling rate in the axial and lateral dimensions, the overall accuracy of the profiles could be increased. The effect of the underestimated length is that the load is underestimated as well, therefore leading to a lower flexural rigidity.

Approximately 2/3 of the cilia were resistant to flow. The cilia were of the same length than the ones shown in Fig. 16, but no clear difference between the loaded and the static condition was seen. An example of such a cilium is shown in Fig. 17. The model has difficulties to predict the profile, because the value of κ becomes very small and the simulation becomes unstable. A possibility to determine the flexural rigidity of the profiles would be to increase the flow rate, and therefore the drag on the cilium. But at flow rates of 500 μL/min and more, cells begin to detach and the profiles could

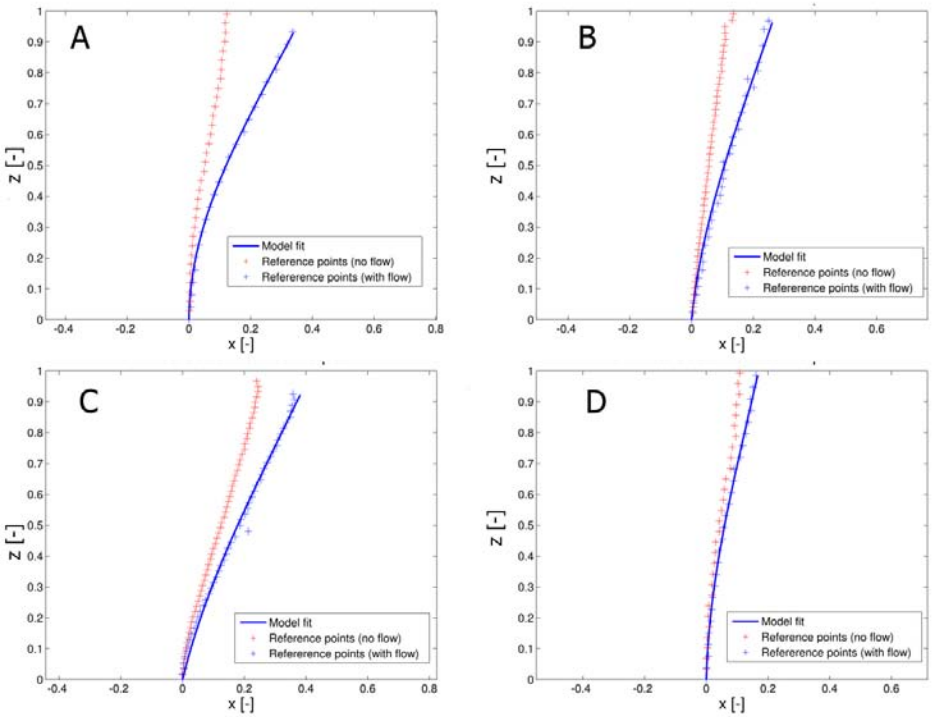

Figure 16: Profiles of four different cilia are shown under flow and no flow, together with the fit of the model. The flow rate is 300 $\mu L/min$ in all cases, but the length of the cilia are not identical, which can't be seen on the figure, as the non-dimensional coordinates are shown. The values for the flexural rigidity, the length and other results are shown in table 2.

not be acquired.

The bending moment experienced at the base of the cilium depends largely on the length of the cilium. Values between 7.8 x 10^{-18} and 6.9 x 10^{-19} Nm were found, for the longest and the smallest cilium respectively. With this measurement, the forces acting on the cytoskeleton can be estimated. If we assume that the force on the cytoskeleton is 0.2 μm distant from the point of rotation, the magnitude of force would be between 3-40 pN.

4.6 Rotation of the cilium

A 7 μm long cilium was imaged under different flow conditions. First the cilium was exposed to 300 μL/min, then to -300, to 200 and lastly to -200 μL/min, where a positive flow is in direction of x. In this case, the cilium was imaged only once per condition, therefore, the profiles are less accurate, especially at the tip. The fluctuations may introduce some errors and difficulties in the interpretation of the results.

There is practically no difference for all four conditions at the lowest 1 μm at the base

Cilium	EI [Nm^2]	$\Delta\theta_{base}[rad]$	ΔL [μm]	L_0 [μm]	Bending Moment [Nm]
a	1.3 x 10^{-24}	0	0.8	3.2	6.9 x 10^{-19}
b	1.9 x 10^{-23}	0	1.1	4.8	2.7 x 10^{-18}
c	1.1 x 10^{-22}	0.1	0.5	5.8	7.8 x 10^{-18}
d	1.2 x 10^{-23}	0	0.3	2.9	9.3 x 10^{-19}

Table 2: Fitting Results. Data corresponds to the cilia shown in Fig. 16. The flexural rigidity EI, the change of angle at the baseΔ θ_{base}, the apparent change in length ΔL, the initial length L_0 and the bending moment are listed.

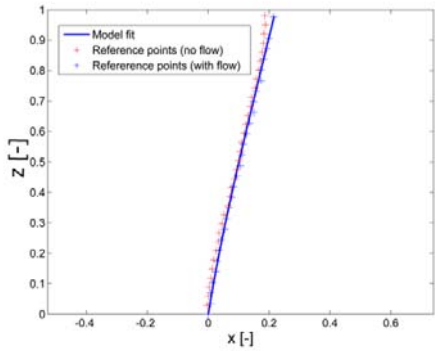

Figure 17: Coordinates and fit of a cilium that doesn't deflect at a shear stress of 150 mPa. Approximately two third of the cilia show this behavior.

of the cilium, but the upper part shows deflection in response to flow. Confusingly, the cilium deflect more when -200 μL/min are applied than at -300 μL/min. With a flow rate of +200 μL/min, the cilium is almost straight, with only the tip deflected in the direction of flow. There is no clear symmetry for the positive and negative flow. From the top-view, one can see that the lower part of the cilium doesn't align completely with the direction of flow (x-axis). There is an angle between the direction of flow and the profile at the base. It looks as if the lower part rotates, but only to a certain degree.

4.7 Immunofluorescent analysis of the ciliary base

The microtubule network and the striated rootlets at the base of the cilium were analyzed by immunocytochemistry. Both structures are known to be associated with the basal body, which builds the origin of the primary cilium. We observed that the base of the cilium is firmly anchored, but also noted that a rotation might occur when the direction of load is changed. The goal of the immunofluorescent imaging of the ciliary base is to determine if there is an asymmetry which could explain the above mentioned observations.

Gamma tubulin can be used to stain the centrioles. This is necessary to find the basal

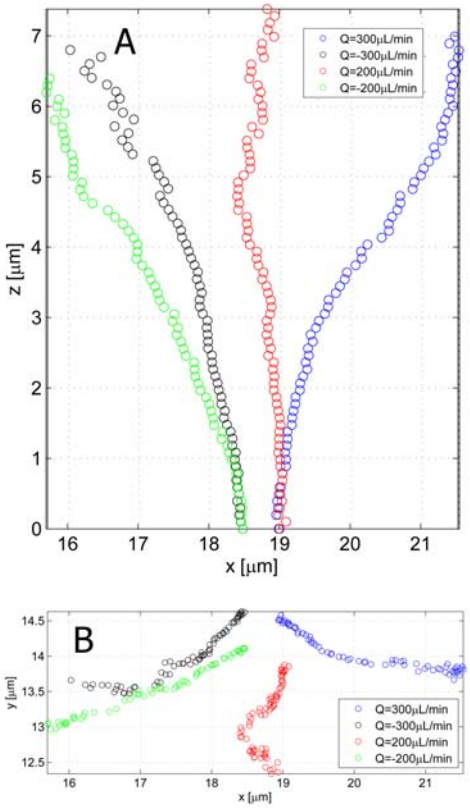

Figure 18: Coordinates of a cilium exposed to different flow rates with (A) showing the side view and (B) the top view. The cilium deflects under flow, and it looks as if the base rotates in the xy-plane.

body, which is one of the two centrioles. Immunocytochemistry showed that the basal body localizes to the base of the cilium, which is labeled with the GFP-SSTR3 fusion protein (Fig. 20A). With immunofluorescence against alpha-tubulin, the connections of the microtubules to the basal body can be seen. The alpha-tubulin antibody stains the cilium as well, so it was possible to find the location of the basal body without the gamma tubulin antibody. By taking the maximum projection of a z-stack at the base of the cilium, the cilium appears as a bright spot. Unfortunately, the quality of the immunostaining differed between repetitions of the experiment and only a few high resolution z-stacks of the ciliary base were obtained. The images were restored by deconvolution. On average, there are five direct connections of the microtubules to the ciliary base. In some case the architecture is clear (Fig. 19 D), whereas in others, the connections are not resolved (Fig. 19 B). The microtubules connected to the basal body form a star-like structure, which is almost symmetric.

The antibody against rootletin, the structural protein of the striated rootlets, was tested on cells fixed with paraformaldehyde and cells fixed with ice-cold methanol. A fluorescent signal was only obtained in the latter case (Fig. 20 B). The fluorescent signal appears at a specific site of the cell, and it extends more in the z-direction than in the lateral dimensions. Unfortunately, the alpha tubulin antibody doesn't work with methanol fixation, therefore, the use of both antibodies at the same time was not successful, and it is not known if the signal of the rootletin antibody is localized to the ciliary base or not. A possibility to answer this question would be to use the gamma-tubulin antibody, that works with both fixation methods. Unfortunately, the secondary for the gamma-tubulin and the rootletin share the same excitation and emission range. Another secondary antibody is needed to determine if the rootletin signal localizes to the ciliary base.

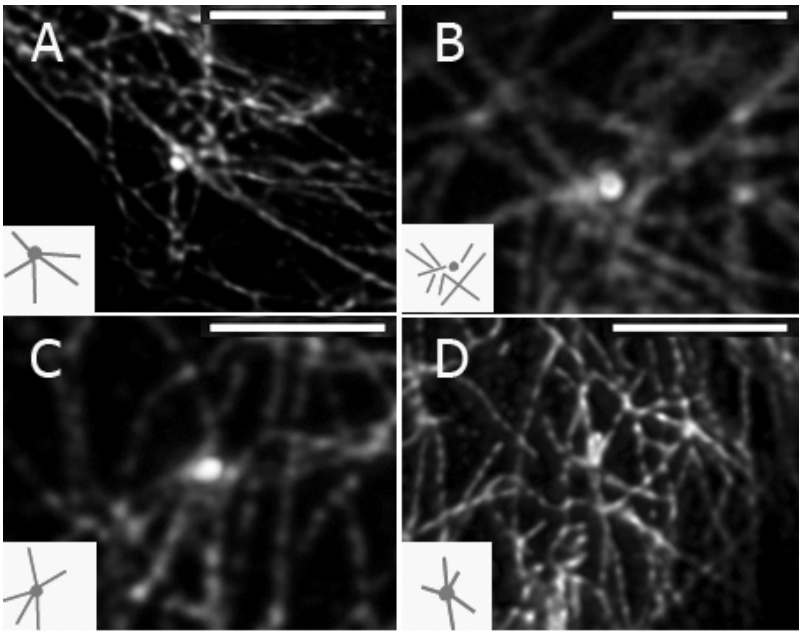

Figure 19: The tubulin network was imaged at the base of the cilium by immunocytochemistry. The location of the base of the cilium was determined by looking for the cilium, which is also stained by the alpha tubulin antibody. Here, a maximum z-projection is shown, and the cilium appears as a bright spot. Inlets show suggested connections of the microtubules to the ciliary base. Some are more evident (D) than others (B). Scale bar 5μm

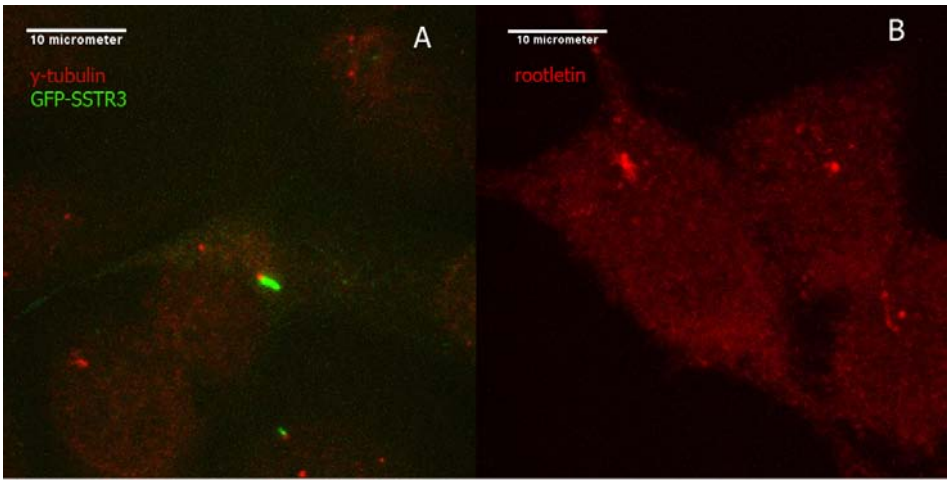

Figure 20: Immunocytochemistry. (A) IMCD cells stained against gamma tubulin, a centrosome marker (in red). The primary cilium is still fluorescent after immunocytochemistry and localizes to one of the centrioles, that is called the basal body. (B) Rootletin localizes to a specific region of the cell, probably to the basal body.

5 Discussion

The model of the primary cilium presented here is novel, because it is valid for large deflections and considers a realistic, linear flow profile. The rotation at the base and the initial curvature is also taken into account for the first time. A linear flow profile is more realistic than a constant, and attempts were made to improve the estimation of the drag by three-dimensional computational fluid dynamics. By fitting the angle at the base θ_{base}, the error between the fit and the reference points decreases. The angle between the cilium and the cell membrane is close, but not equal to 90°. By fitting θ_{base}, the EI value increases compared to a fixed 90° angle assumption which was considered in other models, because some of the deflection can be explained by a simple rotation. Interestingly, θ_{base} doesn't change when flow is applied. This suggests that the base is firmly fixed and that the anchorage provides a high torsional rigidity to the axoneme. The base of the cilium is a hot spot of mechanotransduction. For example, the transmembrane proteins polycystin 1 and two, which are both involved in mechanosensation, localize to the ciliary base. The increase in intracellular Ca^{2+} in response to flow is mediated by these proteins, and a response was observed at the same orders of shear stress we used here [29]. It is not clear how polycystin 1 is activated on a molecular level. It was suggested that the bending of the cilium alters the membrane tension and the local curvature, which could activate the mechanoresponsive proteins. From our observations, the ciliary base doesn't deflect in response to fluid flow at a shear stress of 0.15 Pa. At the given resolution of the confocal imaging system, there is no change in local curvature observed, and as a consequence, the membrane tension most likely doesn't change either. One variable that does change is the stress in the axoneme, but if or how increased stress may lead to a fluid-induced response remains unclear. One problem of comparing results of different studies is that the deflection depends highly on the length of the cilium, which is not the same in different model cell lines.

The flexural rigidity of the primary cilium was previously estimated by Schwartz *et al.*. Their model considers a constant velocity along the length of the cilium, and they report a value of 1.4-1.6 x 10^{-23} Nm^2 [30]. The values obtained by our more sophisticated model show more variability. The bending response and the flexural rigidity of the cilia on IMCD cells differ form cell to cell. If we consider the cilia that deflected in response to the given flow rate, the average EI is close to the values reported by Schwartz.

It is not known if the nine doublet microtubules of the ciliary axoneme are mechanically linked together or not. If we assume that each doublet microtubule acts independently, we would expect an area moment of inertia I_{cilium} of about 9 times bigger than the I_{Mt} value of a microtubule. On the other hand, if we assume that the nine doublet microtubules form a rigid, interconnected structure, the I value can be estimated from electron microscopy images with the following equation: $I = \int y^2 dA$. Numerical integration over the area shown in Fig 21 yields I = 3x$10^{-29}$$m^4$, and a microtubule, approximated as a hollow cylinder with inner and outer radius of 11.5 and 14.2 nm, gives I = 1/4 $\pi(R_o^4 - R_i^4)$ = 2x$10^{-32}$$m^4$ [35]. The area moment of inertia of a cilium might be 1000 times higher than the area moment of inertia of a single

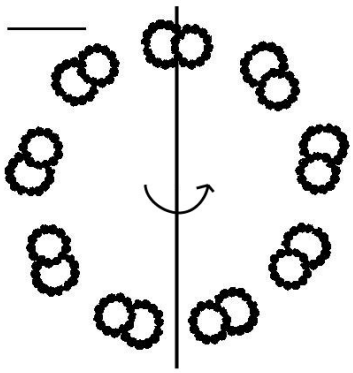

Figure 21: Cross section of a primary cilium. Figure adapted from Hagiwara *et al.* [11]. Scale bar 50 nm

microtubule. The average Young's modulus of elasticity of a microtubule is approximately 2 GPa [24]. From this considerations, a flexural rigidity between 3.6x10^{-22} Nm^2 and 6x10^{-20} Nm^2 can be expected for the primary cilium.

The flexural rigidity obtained by our simulations range from 1.3x10^{-24} to 1.2 x 10^{-22} Nm^2, which is lower than the lower limit of the theoretical considerations. Given that the published values of the flexural rigidity of microtubules vary over orders of magnitude, the theoretical considerations may only be approximately true, and we can assume that the doublet microtubules in the ciliary axoneme behave mechanically independent, at least for the population of cilia that deflected under the given flow rate. The flexural rigidity of the cilia resistant to flow may be considerably higher.

In our model, the drag at the tip of the cilium is not considered. Others added a hemispherical tip to the cylinder, which increases the overall drag [28]. It is not known what the tip of the cilium looks like, but the additional surface exposed to the fluid shear might be important. Therefore, the flexural rigidity measured by our model may underestimate the actual stiffness of the primary cilium.

About 2/3 of the cilia showed a high resistance to flow. This observation suggest that primary cilia don't have homogeneous flexural rigidities. The flow-resistant population of cilia might have a higher flexural rigidity because of mechanical connections between the doublet microtubules. It was also observed that one cilium exposed to different flow rates deflected more at a lower flow rate than at a higher in one direction and that this cilium might have rotated at the base. This rotation may have twisted the axoneme, which may lead to an increased stiffness that depends on the arrangement of microtubules inside the cilium. This hypothesis of passive twisting and rearrangement of the microtubules may also explain the observed variability of the flexural rigidity. It is clear that more data are needed to accurately estimate the flexural rigidity of the primary cilium, and more experiments are needed to test the twisting hypothesis.

The estimation of the bending moment at the base of the cilium depends only on the drag and the profile of the cilium. As a consequence, the values reported are

not as variable as the flexural rigidity. If we consider that the cilium transmits the bending moment to the cytoskeleton, and if we assume that this force acts at 0.2 μm from the point of rotation, the magnitude of the force would be 3-40 pN for the given shear stress. Similar forces were found by Liu *et al.* [19], and forces of this magnitude can induce the breaking of cytoskeletal filaments, or induce conformational changes of structural proteins [36], which may lead to a mechanosensitve signaling response .

The length of the primary cilium is an important parameter for the bending in response to flow. *In vitro*, we observed a slight, but statistically not significant increase in length over time in serum-starved IMCD cells. It was previously reported that primary cilia formation is induced [38] and the length of the cilium is increased in growth arrested cells [15]. The longer the cilium, the more drag it experiences, especially as the drag increases linearly with distance. Therefore, it is plausible that the length of the cilium is regulated to tune the sensitivity to flow. Other investigators observed that the length of the cilium decreases if the cells are exposed to fluid drag by orbital shaking compared to cells cultured under static conditions [28]. Recently, it was shown that the length of the primary cilium is regulated by intracellular calcium or cyclic AMP with a subsequent protein kinase A activation [3]. It is also known that fluid shear induced deflection of the primary cilium decreases intracellular cAMP [16]. Taken together, the cilium length decreases if the cells are exposed to fluid flow, which forms a negative feed-back loop that decreases the sensitivity upon exposure to flow. Our results show the importance of the ciliary length for the deflection in response to flow and the bending moment experienced at the base of the cilium.

Imaging the primary cilium in living cells in 3d with a fast acquisition rate revealed fluctuations of the cilium. The source of the fluctuations remains unclear, but thermal fluctuations can be excluded. This raises interesting questions, which can't be answered yet. Are there active movements of the cilium, or are the fluctuations only an artifact?

The three dimensional reconstruction of the cilium and the cell membrane showed different localizations of the primary cilium. One small cilium was shown to be embedded in the cell membrane. A study by Molla-Herman *et al.* observed a depression of the cell membrane around the base of the cilium using the same cell line and imaging with scanning and transmission electron microscopy [22]. This ciliary pocket was found on 11% of the cilia, and the other 89% of the cilia emerged directly from the surface. In our study, only long cilia were analysed for the estimation of the flexural rigidity, which belong most likely to the latter population. In contrast to the study by Molla-Herman, we were able to image the ciliary pocket in a living cell. With this technique, it would be possible to determine if the observed pocket is a transient structure which appears during ciliogenesis, or if the embedded cilia form a different population of primary cilia.

The structural analysis of the microtubule network around the ciliary base with immunocytochemistry show that approximately five connections exist between the basal body and the tubulin-network. It was reported that there are 1-5 basal feet per basal body in oviductal secretory cells [11], and that there is only one basal foot in motile cilia, which is aligned in the direction of stroke [6]. An asymmetry of bending is

therefore plausible to be a result of an asymmetric arrangement of the connections of the basal body to the tubulin cytoskeleton. Here, we observed a relatively symmetric arrangement of about five connections. It would be interesting to visualize the microtubule network in cells that were analyzed with the bending model and to see if there is a correlation of numbers of connections or orientation of connections with the observed deflection under flow. Given that the microtubule network seems to be symmetric, and given that the ciliary base is tightly anchored, the observed asymmetry of bending could be explained by an asymmetry of the microtubules inside the ciliary axoneme.

6 Conclusion and Perspectives

In conclusion, our novel model that incorporates new features that were observed *in vitro*, such as an initial curvature or an initial tilt, provides a mean to estimate the flexural rigidity of primary cilia. Even if few data was acquired, the results suggest that the flexural rigidity of a cilium is by far more variable than previously thought. Another important result is the fact that the base of the cilium is firmly anchored, at least at the given shear stress of 0.15 Pa. Kidney cells were reported to be sensitive to such orders of shear stress, but it is still not known if the shear stress or if the deflection of the cilium are triggering the mechanosensory response. Our observation is an evidence against the hypothesis, that a local change in curvature activates mechanoresponsive proteins at the ciliary base. But it has first to be proven that the cells we used are indeed sensitive to this order of shear stress, before a conclusion can be made.

More cilia have to be analyzed with this model to characterize the flexural rigidity of the primary cilium. But not only the flexural rigidity can be estimated with the model, but also changes of the bending response, if the underlying structures are manipulated. For instance, one could knock down rootletin, or alternatively destabilize microtubules with colchicine, to determine which structure is responsible for the anchorage of the primary cilium. The model, together with the imaging technique presented, would detect changes in the mechanical behavior of the primary cilium and could potentially lead to new insights in fascinating mechanisms of mechanotransduction.

7 Acknowledgments

First of all, I'd like to thank Prof. Jacobs for giving me the opportunity to work in his lab. His office door was always open and he always took time to answer my questions. This exchange between the EPFL and the Columbia University wouldn't have been possible without my advisor, Prof. Pioletti. I truly thank him for his trust and for having arranged this exchange.

I thank Prof. Hess for his advice on the fluctuation problem and Jun Qiu for helping me with the computational fluid dynamics. Many thanks to my lab mates, Dave, Danny, Matt, Jen, Kristen and An. It was a pleasure to working with you!

References

[1] Charles T Anderson, Alesha B Castillo, Samantha A Brugmann, Jill A Helms, Christopher R Jacobs, and Tim Stearns. Primary cilia: cellular sensors for the skeleton. *Anat Rec (Hoboken)*, 291(9):1074–1078, Sep 2008.

[2] Rommel G. Bacabac, Theo H. Smit, Stephen C. Cowin, Jack J. W. A. Van Loon, Frans T. M. Nieuwstadt, Rob Heethaar, and Jenneke Klein-Nulend. Dynamic shear stress in parallel-plate flow chambers. *Journal of Biomechanics*, 38(1):159 – 167, 2005.

[3] Tatiana Y Besschetnova, Elona Kolpakova-Hart, Yinghua Guan, Jing Zhou, Bjorn R Olsen, and Jagesh V Shah. Identification of signaling pathways regulating primary cilium length and flow-mediated adaptation. *Curr Biol*, 20(2):182–187, Jan 2010.

[4] Oseen C.W. Ueber die stokes'sche formel und ueber eine verwandte aufgabe in der hydrodynamik. *Arkiv For Matematik Astronomi Fysik*, 6:29, 1910.

[5] R. K. Finn. Determination of the drag on a cylinder at low reynolds numbers. *Journal of Applied Physics*, 24(6):771 –773, jun 1953.

[6] D. Frisch and A. I. Farbman. Development of order during ciliogenesis. *Anat Rec*, 162(2):221–232, Oct 1968.

[7] F. Gittes, B. Mickey, J. Nettleton, and J. Howard. Flexural rigidity of microtubules and actin filaments measured from thermal fluctuations in shape. *J Cell Biol*, 120(4):923–934, Feb 1993.

[8] Sarah C Goetz and Kathryn V Anderson. The primary cilium: a signalling centre during vertebrate development. *Nat Rev Genet*, 11(5):331–344, May 2010.

[9] Meral Gunay-Aygun. Liver and kidney disease in ciliopathies. *Am J Med Genet C Semin Med Genet*, 151C(4):296–306, Nov 2009.

[10] Piya Sen Gupta, Natalia V Prodromou, and J. Paul Chapple. Can faulty antennae increase adiposity? the link between cilia proteins and obesity. *J Endocrinol*, 203(3):327–336, Dec 2009.

[11] Aoki Suzuki Takata Hagiwara, Ohwada. The primary cilia of secretory cells in the human oviduct mucosa. *Medical Molecular Morphology*, 41(4):193–198, December 2008.

[12] J.T. Holden. On the finite deflections of thin beams. *International Journal of Solids and Structures*, 8(8):1051 – 1055, 1972.

[13] Isao Imai. A new method of solving oseen's equations and its application to the flow past an inclined elliptic cylinder. *Proceedings of the Royal Society of London. Series A, Mathematical and Physical Sciences*, 224(1157):141–160, 1954.

[14] Donald E Ingber. Cellular mechanotransduction: putting all the pieces together again. *FASEB J*, 20(7):811–827, May 2006.

[15] Enko N Kiprilov, Aashir Awan, Romain Desprat, Michelle Velho, Christian A Clement, Anne Grete Byskov, Claus Y Andersen, Peter Satir, Eric E Bouhassira, Sren T Christensen, and Rhoda Elison Hirsch. Human embryonic stem cells in culture possess primary cilia with hedgehog signaling machinery. *J Cell Biol*, 180(5):897–904, Mar 2008.

[16] Ronald Y Kwon, Sara Temiyasathit, Padmaja Tummala, Clarence C Quah, and Christopher R Jacobs. Primary cilium-dependent mechanosensing is mediated by adenylyl cyclase 6 and cyclic amp in bone cells. *FASEB J*, Apr 2010.

[17] H. Lamb. On the uniform motion of a sphere through a viscous fluid. *Philosophical Magazine*, 21:112–121, 1911.

[18] Madeline A Lancaster and Joseph G Gleeson. The primary cilium as a cellular signaling center: lessons from disease. *Curr Opin Genet Dev*, 19(3):220–229, Jun 2009.

[19] Wen Liu, Shiyun Xu, Craig Woda, Paul Kim, Sheldon Weinbaum, and Lisa M. Satlin. Effect of flow and stretch on the [ca2+]i response of principal and intercalated cells in cortical collecting duct. *Am J Physiol Renal Physiol*, 285(5):F998–1012, 2003.

[20] Amanda M. D. Malone, Charles T. Anderson, Padmaja Tummala, Ronald Y. Kwon, Tyler R. Johnston, Tim Stearns, and Christopher R. Jacobs. Primary cilia mediate mechanosensing in bone cells by a calcium-independent mechanism. *Proceedings of the National Academy of Sciences*, 104(33):13325–13330, 2007.

[21] Edward J Michaud and Bradley K Yoder. The primary cilium in cell signaling and cancer. *Cancer Res*, 66(13):6463–6467, Jul 2006.

[22] Anahi Molla-Herman, Rania Ghossoub, Thierry Blisnick, Alice Meunier, Catherine Serres, Flora Silbermann, Chris Emmerson, Kelly Romeo, Pierre Bourdoncle, Alain Schmitt, Sophie Saunier, Nathalie Spassky, Philippe Bastin, and Alexandre Benmerah. The ciliary pocket: an endocytic membrane domain at the base of primary and motile cilia. *J Cell Sci*, 123(Pt 10):1785–1795, May 2010.

[23] S.M. Nauli, F.J. Alenghat, Y. Luo, E. Williams, P. Vassilev, X. Li, A.E.H. Elia, W. Lu, E.M. Brown, S.J. Quinn, et al. Polycystins 1 and 2 mediate mechanosensation in the primary cilium of kidney cells. *Nature genetics*, 33(2):129–137, 2003.

[24] Francesco Pampaloni and Ernst-Ludwig Florin. Microtubule architecture: inspiration for novel carbon nanotube-based biomimetic materials. *Trends in Biotechnology*, 26(6):302 – 310, 2008.

[25] Francesco Pampaloni, Gianluca Lattanzi, Alexandr Jons, Thomas Surrey, Erwin Frey, and Ernst-Ludwig Florin. Thermal fluctuations of grafted microtubules provide evidence of a length-dependent persistence length. *Proc Natl Acad Sci U S A*, 103(27):10248–10253, Jul 2006.

[26] H. A. Praetorius and K. R. Spring. Bending the mdck cell primary cilium increases intracellular calcium. *J Membr Biol*, 184(1):71–79, Nov 2001.

[27] V. Ramamurthy and M. Cayouette. Development and disease of the photoreceptor cilium. *Clin Genet*, 76(2):137–145, Aug 2009.

[28] Andrew Resnick and Ulrich Hopfer. Force-response considerations in ciliary mechanosensation. *Biophysical Journal*, 93(4):1380 – 1390, 2007.

[29] Susanna Rydholm, Gordon Zwartz, Jacob M Kowalewski, Padideh Kamali-Zare, Thomas Frisk, and Hjalmar Brismar. Mechanical properties of primary cilia regulate the response to fluid flow. *Am J Physiol Renal Physiol*, Jan 2010.

[30] E. A. Schwartz, M. L. Leonard, R. Bizios, and S. S. Bowser. Analysis and modeling of the primary cilium bending response to fluid shear. *Am J Physiol Renal Physiol*, 272(1):F132–138, 1997.

[31] E. Scott Seeley and Maxence V Nachury. The perennial organelle: assembly and disassembly of the primary cilium. *J Cell Sci*, 123(Pt 4):511–518, Feb 2010.

[32] G.G. Stokes. On the effect of the internal friction of fluids on the motion of pendulums. *Transactions of the Cambridge Philosophical Society*, 9:8, 1851.

[33] Sara Temiyasathit and Christopher R Jacobs. Osteocyte primary cilium and its role in bone mechanotransduction. *Ann N Y Acad Sci*, 1192(1):422–428, Mar 2010.

[34] D. J. Tritton. Experiments on the flow past a circular cylinder at low reynolds numbers. *Journal of Fluid Mechanics*, 6(04):547–567, 1959.

[35] P Venier, A C Maggs, M F Carlier, and D Pantaloni. Analysis of microtubule rigidity using hydrodynamic flow and thermal fluctuations. *Journal of Biological Chemistry*, 269(18):13353–13360, 1994.

[36] Viola Vogel and Michael Sheetz. Local force and geometry sensing regulate cell functions. *Nat Rev Mol Cell Biol*, 7(4):265–275, Apr 2006.

[37] Robert H Webb. Confocal optical microscopy. *Reports on Progress in Physics*, 59(3):427, 1996.

[38] Di Zhu, Shuo Shi, Hongzhong Wang, and Kan Liao. Growth arrest induces primary-cilium formation and sensitizes igf-1-receptor signaling during differentiation induction of 3t3-l1 preadipocytes. *J Cell Sci*, 122(Pt 15):2760–2768, Aug 2009.